Title

Polarization-resolved black phosphorus/molybdenum disulfide mid-wave infrared photodiodes with high detectivity at room temperature

Journal

Nature Photonics, 12(10)

ISSN

1749-4885

Authors

Bullock, James
Amani, Matin
Cho, Joy
et al.

Publication Date

2018-10-01

DOI

10.1038/s41566-018-0239-8

Peer reviewed

Polarization Resolved bP / MoS_2 Mid-Wave Infrared Photodiodes with High Detectivity at Room Temperature

James Bullock[1,2‡], Matin Amani[1,2‡], Joy Cho[1,2], Yu-Ze Chen[3], Geun Ho Ahn[1,2], Valerio Adinolfi[1,2], Vivek Raj Shrestha[4], Yang Gao[5], Kenneth B. Crozier[4,5], Yu-Lun Chueh[3] and Ali Javey[1,2,*]

[1]*Department of Electrical Engineering and Computer Sciences, University of California, Berkeley, California 94720, USA.*

[2]*Materials Sciences Division, Lawrence Berkeley National Laboratory, Berkeley, California 94720, USA.*

[3]*Department of Materials Science and Engineering, National Tsing Hua University, Hsinchu, Taiwan 30013, R.O.C.*

[4] *School of Physics, University of Melbourne, VIC 3010, Australia*

[5] *Department of Electrical and Electronic Engineering, University of Melbourne, VIC 3010, Australia*

‡ *These authors have contributed equally to this work*

* *corresponding author: Ali Javey (ajavey@berkeley.edu)*

Infrared (IR) photodetectors are currently subject to a rapidly expanding application space, with an increasing demand for compact, sensitive, and inexpensive detectors. Despite continued advancement, technological factors limit widespread usage of IR detectors; specifically, the need for cooling and high costs associated with processing of III-V/II-VI semiconductors. Here, black-phosphorous (bP) / MoS_2 heterojunction photodiodes are explored as mid-wave infrared (MWIR) detectors. While previous studies have demonstrated photodiodes using bP, here we significantly improve the performance, showing for the first time that such devices can be competitive with conventional MWIR photodetectors. By optimizing the device structure and light management, we demonstrate a two-terminal device which obtains room temperature external quantum efficiencies (η_e) of 35% and specific detectivities (D^*) as high as 1.2×10^{10} cmHz$^{1/2}$W^{-1} in the MWIR region. Furthermore, by leveraging the anisotropic optical properties of bP we demonstrate the first bias-selectable polarization resolved photodetector which operates without the need for external optics.

Infrared (IR) photodetectors are essential components in a host of fields, including medical, scientific, communication, automation and surveillance.[1,2] The majority of today's commercially available, high performance IR photodetectors are made using III-V and II-VI absorbers, for example, $In_{1-x}Ga_xAs$, InSb, and $Hg_{1-x}Cd_xTe$.[3] While significant progress has

greatly increased their application, a number of drawbacks limit wider utilization of IR photodetectors. Most notably, these devices typically rely on expensive growth methods and require active cooling to reduce thermal noise. The latter is particularly crucial for narrow bandgap absorbers operating in the mid-wave infrared (MWIR, 3-5 μm) and long wave infrared (LWIR, 8-12 μm) spectral bands where cryogenic cooling is typically required to achieve high performance. In addition, several specific applications cannot be directly addressed using detectors fabricated from traditional material systems. An example of this is detection of the polarization state of light, which is utilized in numerous specialized applications including astronomy, polarization-division multiplexing and remote sensing. Normally detectors used for this application require either polarization optics or multiple devices arranged in a side-by-side configuration, which adds system complexity and limits the resolution for imaging purposes. Furthermore, while numerous materials, most notably nanowires, show polarized absorption, a polarization resolved detector has yet to be demonstrated. As such, there is considerable interest in the exploration of new IR absorber materials which offer the potential to address these shortcomings and can be applied in novel device architectures.

Two-dimensional (2D) materials have shown initial promise for use in future IR photodetectors.[4,5] One of the key advantages offered by 2D layered crystals is their out-of-plane van der Waals bonding which allows the use of thin layers without suffering from detrimental effects such as surface

dangling bonds. This advantage is particularly important in infrared detectors where thin absorbers can reduce noise resulting from generation-recombination, a strategy which is often not permitted in traditional semiconductors due to surface recombination. Furthermore, the van der Waals bonding in these materials allows for the construction of heterojunctions without consideration of factors such as lattice matching or deposition temperature; providing a significant advantage over traditional three-dimensional materials. Black phosphorus (bP), an elemental 2D material, has recently garnered a significant amount of attention within the optoelectronic community.[5–7] This interest is partially based on the anisotropic optoelectronic properties of bP, which result in polarization dependent absorption.[7,8] Black phosphorus also exhibits a thickness tuneable direct bandgap, between the near infrared ($E_g \approx 1.5$ eV) for monolayers to the MWIR ($E_g \approx 0.3$ eV) in the case of bulk.[7,8] In addition, several studies have demonstrated that bP can be effectively combined with transition metal dichalcogenides including MoS_2,[9–11] WSe_2,[12] and ReS_2,[13] to form a range of functional van der Waals heterojunctions. To date, numerous photodetectors utilizing bP have been demonstrated indicating its promise as a next-generation IR detector platform.[14–16] Among these, a number of preliminary studies have shown the potential of the bP / MoS_2 heterojunction in this application.[9–11] However, devices presented thus far show inferior performance to existing IR room temperature photodetectors, with reported external quantum efficiency values of less than 5%; and are characterized

only at discrete wavelengths either in the near infrared or short-wave infrared bands.

Here we utilize bP / MoS_2 heterostructures to fabricate photodiodes and optimize the devices for detection of MWIR light intensity and polarization at room temperature. To optimize the collection of light, we perform in-depth characterisation of bP, and report, for the first time, the complex refractive index of this material in a wavelength range that encompasses the MWIR. This information is used to design and fabricate a simple optical structure which deliberately utilizes destructive interference to efficiently couple in a narrow band of MWIR light – permitting the demonstration of a high quantum efficiency bP / MoS_2 photodiode. Finally, we demonstrate a bias-selectable polarization resolved bP photodetector, utilizing two orthogonally aligned bP / MoS_2 photodiodes, monolithically integrated to create a device which directly measures both the intensity and polarization of incoming MWIR light.

Results and discussion

Black phosphorus mid-wave infrared photodiode design. Two primary figures of merit for photodetectors are their external quantum efficiency (η_e) and specific detectivity (D^*). These parameters are optimized by increasing the percentage of incident photons which generate photocurrent as well as via reduction of the electronic noise. As such, simultaneous optimization of η_e and D^* requires consideration of both optical and electrical design. A schematic showing the structure of the

heterojunction photodiodes fabricated in this work as well as an example optical micrograph are shown in Fig. 1a and 1b, respectively. The device consists of a bP / MoS_2 heterojunction where a thin (~10-20 nm) n-type MoS_2 layer acts as an electron selective-contact and MWIR window. Holes are contacted via a rear Au pad, which simultaneously acts as a MWIR back reflector. As shown schematically in the simulated band diagram of Fig 1c, the MoS_2 heterojunction provides asymmetric band offsets with the bP, allowing the flow of electrons to the MoS_2 contact while blocking the flow of holes. A false coloured transmission electron micrograph (TEM) of a completed device is shown in Fig. 1d. In addition, high resolution TEM images of the bP / MoS_2 and bP / Au interfaces are shown in Fig. 1e and 1f, respectively. The layered structure of bP and MoS_2 can be seen with corresponding monolayer thicknesses of 5.5 Å and 6 Å, respectively. A thin amorphous layer can also be observed at both interfaces, most prominently at the bP / Au interface, and is attributed to PO_x which forms during device fabrication. This layer could potentially improve hole collection at the bP / Au interface because of its known p^+ character which may reduce the hole contact resistivity. However, its growth at the bP / MoS_2 interface would ideally be avoided to prevent the formation of an electron barrier which could result in a reduced collection efficiency.

Refractive index extraction and optical optimization. Losses due to reflection limit the fraction of incident light that can be absorbed and are a strong function of both the bP and MoS_2 layer thicknesses. The reflection and

absorption in the device can be modelled utilizing the complex refractive index (n, k) of the two materials. While broadband values of n and k have been reported for MoS_2, only the visible refractive index has been characterized for bP to date.[17] The anisotropic crystalline structure of bP, shown in Fig 2a, results in polarization dependent optical properties (referred to as linear dichroism). Light impinging with an electrical field parallel to the x-axis, or arm-chair direction, sees a sharp absorption onset at the bulk bP band edge of ~0.31 eV.[6,7,18] Absorption of polarized light aligned to the y-axis or zig-zag direction, however, is symmetry-forbidden at the ~0.31eV band edge and substantially weaker at higher energy wavelengths.[7,8,19] This has been confirmed experimentally for bulk bP from MWIR to visible wavelengths.[5,7,20] To extract an effective n and k for the x-and y-directions in bP, polarized IR reflection measurements were performed on bP crystals with varying thickness, ranging from 50 nm to 500 nm, on Au substrates. Example reflection data at individual thicknesses is included in Supplementary Information S1. The combined interpolation of these polarized reflection measurements is shown in Fig. 2b and 2c for incident polarisations aligned along the x- and y-axis of bP, respectively.

For polarized illumination aligned to the x-direction, a clear drop in reflection can be seen at photon energies above 0.31 eV for all thicknesses. This is a result of the onset of absorption at the band edge of bP. As expected, no such sharp step is seen for the y-direction in Fig. 2c. Refractive index values are obtained using the transfer matrix method[17] to fit a model

of the thickness (t) dependent reflection $R_{model}(t)$ to the measured reflection $R_{meas}(t)$ at each wavelength. The model is based on a bP / Au stack and assumes that the refractive index is thickness independent across the measured thickness range (50 – 500 nm). This assumption is based on the predicted saturation of the layer dependent band-structure of bP above ~8 layers,[6] and also further demonstrated by fitted reflection measurements in Supplementary Material S1. The extracted n and k values for the x-direction and y-direction are provided in Fig. 2d and 2e, respectively. For light polarized in the x-direction a pronounced step in the extinction coefficient, k, is observed at λ = 3.8 μm which corresponds well to the expected band edge of bP. More details of the indices extraction process can be found in Supplementary Material S1.

With these n and k values, we use the transfer matrix method to simulate the absorption of the photodiode in the x-direction. Ideally from an electrical standpoint, the thickness of the bP layer should be minimized in order to reduce noise resulting from generation-recombination as well as to improve the carrier extraction efficiency. However, from an optical perspective, absorption within the bP layer, which is small for very thin layers, should be maximised. To obtain a compromise between these two requirements, the bP absorption, averaged between λ = 2.5-3.8 μm, is simulated as a function of the bP and MoS_2 layer thicknesses. A contour plot of the modelled absorption is provided in Fig. 2f. The periodic absorption behaviour is associated with changes in front surface reflection due to

thickness dependent constructive and destructive interference of MWIR light. A local maximum in absorption is seen for bP layers with a thickness of 170 nm on Au, with an MoS_2 thickness of zero. This corresponds to the expected quarter wavelength minima in reflection, and hence interference effects can be used to provide a compromise between minimising thickness and maximising absorption. Given that an MoS_2 layer with sufficient lateral conductivity is required to collect electrons, we choose an optimum device configuration of bP (~150 nm) / MoS_2 (15 nm). With this optical design ~80% of incident light polarized in the *x*-direction at λ = 3 μm can be absorbed in the bP layer. We emphasize that, in terms of device thickness, this detector bridges the gap between conventional 2D material photodetectors and traditional bulk semiconductor detectors. Resultantly, it inherits benefits from both of these two detector classes, such as increased absorption as well as being free of surface dangling bonds.

Photodiode characterization. The *IV* characteristics of a typical bP / MoS_2 heterojunction photodiode, measured at 300 K with no illumination, is provided in Fig. 3a and shows the expected rectifying behaviour of a diode formed using a narrow bandgap material. The inset of Fig. 3a compares the measured *IV* behaviour with and without illumination from a 1000 K unpolarized blackbody source. The generation of photocarriers shifts the *IV* curve downwards, resulting in an open circuit voltage V_{oc} and short circuit current I_{sc}, confirming that the device is operating in the photovoltaic mode. Figure 3b shows the relationship between the short circuit current density J_{sc}

and incident optical power density from a λ = 2.7 μm laser diode source. The device shows the expected linear increase in photocurrent as a function of incident light power density over the full measurement range, which spans five orders of magnitude. Similar results are found using a λ = 1.6 μm illumination source as shown in Supplemental Information S5.

The quantum efficiency of the device is measured under *x*-direction polarized illumination using a calibrated Fourier transform infrared spectrometer (FTIR), the setup of which is described in the Methods section. As shown in Fig 3c, the bP / MoS_2 photodiode shows an external quantum efficiency η_e of ~30-35% from λ=2.5-3.5 μm. These are the highest η_e values reported for bP in this range at room temperature and correspond to current responsivity values of ~0.9 A/W (see Supplemental Information S3). Also presented in Fig 3c is the measured reflection *R*, plotted as 100%-*R*. The narrow spectral band of MWIR light coupled into the absorber corresponds to the targeted quarter wavelength interference feature with its peak occurring just below λ=3 μm. From η_e and *R*, the internal quantum efficiency (η_i) can also be calculated according to: $\eta_i(\lambda)=\eta_e(\lambda)/$¿), yielding a value of 40-50% at room temperature. The polarization dependence of η_e at λ = 3.5 μm, as a function of polarization angle, is provided in the polar plot of Fig. 3d. It can be seen that as the polarization angle is changed from 0° (aligned with the *x*-axis) to 90° (aligned to the *y*-axis) a decrease in η_e, from greater than 30% to less than 1%, is measured. An example $\eta_e(\lambda)$ comparison, across the MWIR spectral range, for these two polarization angles is included in the

Supplementary Information S3. That the η_e for *x*-polarized light is substantially higher than for *y*-polarized light is consistent with the anisotropic absorption discussed in Fig. 2 and is in alignment with previous responsivity measurements of bP photodetectors at shorter wavelengths.[7]

As shown in Fig. 3e, the η_e shows no significant changes in spectral shape as a function of temperature, apart from a small red-shift in the absorption edge, attributed to a decrease in the bandgap with decreasing temperature. This anomalous temperature dependence of the bandgap has been previously predicted and experimentally observed in bP.[18,19] However, η_e increases as the temperature is decreased, reaching a value of 63% at 78 K. This is further illustrated in the inset of Fig 3c, with η_e and η_i (measured at λ = 3 μm) plotted as a function of inverse temperature, showing that η_i reaches a peak value of 84% at 100 K. This is most likely a result of an increase in the minority carrier diffusion length at lower temperature. For a device where the back contact is several minority carrier diffusion lengths (L_d) away from the junction, the internal efficiency can be calculated using:

$$\eta_i = (1 - R(\lambda)) \frac{\alpha(\lambda) L_d}{1 + \alpha(\lambda) L_d} \quad (1)$$

where α is the absorption coefficient. The increase in η_i from 300 K to 77K observed here, is consistent with Hall mobilities measured for bP ($\mu_{h,300k} \approx$ 750 $cm^2V^{-1}s^{-1}$, $\mu_{h,77k} \approx$ 3,800 $cm^2V^{-1}s^{-1}$).[24]

To directly compare the performance of the bP / MoS_2 photodiode to conventional photodetectors, we extract its specific detectivity D^*. This is achieved utilizing two independent approaches, which are discussed in detail in the Methods section. Firstly, D^* is calculated, following the approach suggested in Ref[3] for a photodiode under 0 V bias, from η_e and the zero-bias resistance area product (R_0A):

$$D^* = \frac{\eta_e \lambda q}{hc}\left[\frac{4kT}{R_0 A} + 2q^2 \eta_e \Phi_b\right]^{-1/2} \quad (2)$$

where λ is the wavelength, q is the elementary charge, c is the speed of light in vacuum, T is the detector temperature, Φ_b is the background flux density and h and k are the Planck and Boltzmann constants. The second term in the parenthesis accounts for contributions to noise from fluctuations in the thermal background and is negligible in this case, since $4kT/R_0A > 2q^2\eta\Phi_b$. Figure 3f shows $D^*(\lambda)$ extracted from this approach at room temperature compared against the current state-of-the-art room temperature photodiodes,[21,22] many of which are commercially available. It can be seen that the bP photodiode outperforms more established technologies in the MWIR region, with a peak D^* of 1.2×10^{10} cmHz$^{1/2}$W^{-1} at λ = 3.8 μm. It should be noted that the MoS_2 / bP photodiode presented in Figure 3 has been characterized at 0 V bias, unlike many of the detectors presented in Figure 3f, which require an applied bias to obtain the reported values. To verify the MoS_2 / bP photodiode D^* values, the noise equivalent power (NEP) was measured for this device under flood illumination from a blackbody source as

described in Supplementary Information S4. In this approach the incident power density is calculated using geometrical considerations, the temperature of the source and an integration of the total irradiance to the band edge.[23] Additionally, the noise is directly measured allowing D^* to be calculated as $\sqrt{A\,\Delta f}/NEP$, where Δf is the integration time (1 second). From this measurement, we find a room temperature D^* value of 7×10^9 cmHz$^{1/2}$W^{-1}. This value is in good agreement with the spectral D^*, calculated from the device R_0A shown in Fig. 3f. Further information on the D^* for these detectors, including its temperature dependence, can be found in Supplementary Information S3 and S4.

The frequency response and noise current for the bP / MoS_2 heterojunction photodiodes is characterized in Fig. 4. As shown in Fig. 4a no observable baseline drift in photoresponse is observed under modulated laser diode illumination (λ = 2.7 μm). In addition, the rise and fall times, measured under λ = 2.7 μm illumination at 0 V bias, are found to be 3.7 μs and 4 μs, respectively as shown in Fig. 4b. These values are among the fastest reported for bP based photoconductors and photodiodes.[13,15,24] While this is slower than commercially available MWIR photodiodes,[29] these values are promising given the early stage of device development and are faster than common photoconductive and thermal detectors, as shown in Supplementary Table S2. The dashed purple lines in Fig. 4b, measured from a commercially available InAs photodiode, are included to provide a reference of the instrument response. Similar rise / fall times are found when

an illumination source of λ = 1.6 μm is used, as shown in Supplementary Information S5. Figure 4c shows the measured frequency response, with the 3 dB point at approximately 100 kHz using a λ = 1.6 μm illumination source. Fig. 4f shows the measured noise current spectrum of the bP / MoS_2 photodiode. The shape it exhibits is commonly seen in systems dominated by generation-recombination noise. Notably 1/*f* noise behaviour is not observed at low frequencies since the device is operated in photovoltaic mode at zero bias.[30]

Polarization-resolved, bias-selectable photodetector. Finally, we leverage this device structure and the anisotropic optical properties of bP to develop a polarization resolved detector. A schematic of the polarization resolved detector developed in this study is shown in Fig. 5a and a false coloured TEM cross-section of a fabricated device is shown in Fig. 5b. The device consists of two vertically stacked bP layers arranged so that their crystal orientations are perpendicular to one another. These two bP layers are separated by a common MoS_2 electron contact and each bP layer has an isolated hole contact. This configuration is similar to two-colour back-to-back photodiodes which have been previously demonstrated with III-V semiconductors.[31] The bottom bP layer utilizes a full-area Au hole contact, similar to the photodiodes presented above, while the top bP layer collects holes through a MoO_x / Pd hole contact adjacent to the back reflector. The MoO_x / Pd stack has been shown to be an effective hole contact to a number of semiconductor materials,[32,33] owing to its large work function.

To demonstrate the performance of this device, spectrally resolved photoresponse measurements are taken individually on the top and bottom bP photodetectors using the circuit configuration shown in Fig 5c *i* and *ii*, respectively. Each device is measured under two conditions: linearly polarized light aligned to the *x*-axis of the top device (90°) and, linearly polarized light aligned to the *x*-axis of bottom device (0°). All four measurements are provided in Fig. 5d. The performance of this device can be quantified by an extinction ratio r_e for each layer, defined as the photoresponse measured with *x*-polarized illumination divided by photoresponse for *y*-polarized illumination. For both the top and bottom devices r_e values of ~100:1 are calculated at λ = 3.5 μm, which is on the order of the extinction ratio of the polarizer used in this study. These results are further corroborated by the polar plot of Fig. 5e, which shows the photoresponse as a function of polarizer angle at λ = 3.5 μm. In separate measurements, presented in Supplementary Information S6, it is shown that the device is also able to simultaneously detect the two linear polarization components when illuminated with unpolarized light. Furthermore, the response from the individual detectors can be accessed in a bias-selectable (*i.e.* two-terminal configuration) as depicted in the circuit schematic of Fig 5c *iii*. By applying a bias of ±250 mV across the outer contacts one device is reverse biased (where the photocurrent is collected), and the other forward biased (contributing negligibly to the photocurrent). Note that for these measurements the MoS_2 contact was electrically disconnected. The

functionality of this configuration is clearly seen in Fig. 5f by the exclusive collection of only 0° or 90° linear polarized MWIR light under negative or positive biasing, respectively. A bias of ±250 mV was chosen as it was the minimum value at which photocurrent from the two detectors could be effectively separated. Higher biases were avoided to minimise noise due to dark current in the device. The unbalanced photocurrent from the top and bottom bP layers can be attributed to a combination of device variation and differences in absorption arising from the layer thicknesses and their position within the device stack. An optical structure, which couples in and absorbs an equal proportion of perpendicularly polarized light in the two bP absorbers, can be realized by controlling the bP and MoS_2 layer thicknesses and integrating an antireflection layer.

Conclusion

In summary, we have designed and fabricated MWIR bP / MoS_2 heterojunction photodiodes with high performance at room temperature. By determining the complex refractive index in the IR, we have designed a simple optical structure for the bP / MoS_2 photodiode that achieves high MWIR absorption via interference. This allows the use of a moderately thin bP layer (~150 nm), which reduces noise while still permitting high absorption (in excess of ~80%) within a narrow band in the MWIR region. These devices display impressive room temperature η_e and D^* values of 35% and 1.2×10^{10} $cmHz^{1/2}W^{-1}$, respectively. Finally, we utilize the anisotropic optical properties of bP to demonstrate a bias-selectable polarization-resolved monolithic

photodetector, which is capable of simultaneously detecting orthogonally polarized light without the use of external optics. This could further be expanded upon to create polarimetry focal plane arrays which do not rely on moving parts or additional optical components.

Methods

Refractive index extraction and optical simulations. Samples for refractive index extraction were fabricated by thermally evaporating Ti / Au (5/80 nm) onto a Si/SiO_2 carrier wafer. Following this, bP (Smart Elements) was mechanically exfoliated onto the Au surface in an N_2 purged glovebox. A set of 22 bP flakes were chosen with approximately linearly spaced thickness from 50 to 500 nm, as measured by atomic force microscopy (AFM) (Bruker Dimension Icon). Polarized reflection measurements were taken using a Fourier transform infrared (FTIR) microscope (Thermo Scientific, Nicolet iS50) with a BaF_2 wire grid linear polarizer (Thorlabs). The arm-chair direction of the bP absorber was determined by measuring reflection as a function of polarization, to find the angle at which maximum absorption occurs. Implicit in this approach is the assumption that the largest absorption will occur when light is aligned to the *x*, or arm-chair direction, a fact that has been theoretically predicted and demonstrated by a number of previous studies.[7,34,35] In all cases the minimum absorption (at 0.31 eV) was found to be offset by 90° from this angle, corresponding to the expected zig-zag or *y*-direction. All FTIR reflection measurements in this study utilize a bare Au surface as a 100% reflection standard. The set of reflection curves in the *x*-

direction were fitted using the transfer matrix method, which models the reflection of the bP / Au stack using the refractive indices of bP as the only fitting parameter. The optical simulations of the full bP / MoS_2 / Au photodiodes were also performed through the transfer matrix method utilizing known refractive index values for Au, constant values for MoS_2 (n = 4.3, k = 0), as well as the refractive index values for bP measured in this work. An average of the bP absorption values over the λ = 2.5-3.8 μm range was obtained for every combination of MoS_2 and bP thicknesses.

Device fabrication. Photodiodes presented in this work were fabricated by a dry transfer process utilizing a poly(methyl methacrylate) (PMMA) carrier. A detailed description of this process can be found in Supplemental Information S2. In brief, freshly exfoliated bP and MoS_2 sheets are transferred onto an Au pad creating an Au / bP / MoS_2 stack. A contact to the MoS_2 layer was then patterned by e-beam lithography and a 40 nm thick Ni film was subsequently deposited by thermal evaporation. In some devices, the heterojunction was patterned by e-beam lithography and subsequently etched in a Xactix vapor etching tool by XeF_2.[36] Finished devices were encapsulated by an ~2 nm thick AlO_x layer formed by thermal evaporation of Al. Example micrographs taken during the above process steps is provided in Supplementary Figure S2. A discussion of the assumptions made for the area of the device is provided in Supplementary Information S2.

For the polarization resolved detector, an identical dry transfer process was used to create an MoS_2 / bP / Au stack. An additional bP flake was transferred

on top of the MoS_2 layer such that its crystal orientation was orthogonal to the bottom bP layer. The crystalline orientations of the bP sheets was determined using polarized reflection measurements performed in an FTIR microscope as described above. The hole contact for the top bP device was patterned using electron beam lithography, followed by evaporation of MoO_x / Pd (4/30 nm). For all devices in this study, care was taken to reduce air exposure during fabrication of devices to minimize PO_x growth at the bP surface. Processing steps including bP exfoliation, lift-off, PMMA removal and AFM were all performed in either a glovebox or a nitrogen purged environment and all chemicals used were anhydrous. For measurements of surface oxidation prevention in fabricated devices please see Supplementary Information S3.

Device characterisation. Finished devices were wire-bonded into 24 pin chip-carriers which were in turn mounted into a cryostat with a CaF_2 window and measured at a base pressure < 10^{-5} Torr. Current-voltage measurements were taken in a 2-probe configuration, under vacuum using an Agilent Technologies B1500A semiconductor device analyser. Spectral response and η_e were characterized at I_{sc} (i.e. 0 V bias) by placing the cryostat at the auxiliary exit port of the FTIR. The sample was then excited using modulated illumination from a Globar (1000 K blackbody). The resulting photocurrent was then sent to a current amplifier (Stanford Research Systems SRS570) and subsequently returned to the external detector interface of the FTIR. For polarization resolved measurements, a BaF_2 wire grid linear polarizer was

placed in the beam path. The FTIR system was calibrated using two reference detectors: a NIST calibrated Ge photodiode is used to measure the source intensity at the outlet and an inbuilt deuterated-triglycine sulfate (DTGS) detector is used to measure the relative spectral intensity of the source. Further information on the FTIR setup is provided in Supplementary Information S3. Additionally, the detectivity values are confirmed using a blackbody setup with flood illumination. Here the device is excited using a chopper-modulated blackbody (temperature range 473 to 673 K) with no additional optics besides the cryostat window; the incident power density here is calculated using Planck's law and geometrical considerations, *i.e.* aperture size and sample to blackbody distance. Further details on this process can be found in Supplementary Information S4 and in Ref.[23] Reflection measurements are performed in an attached FTIR microscope, with the wire grid polarizer placed in the incoming beam path. The rise/fall times and linearity of the device were characterized using illumination from a λ = 2.7 µm laser diode. For rise/fall measurements the laser diode was directly modulated with a square waveform, and the instrument response was measured using a commercial InAs photodiode. For frequency response measurements a SRS570 current amplifier in high-bandwidth mode with a gain >20 µA/V was used (corresponding to a bandwidth of 1 MHz). For dynamic range measurements the laser was directly modulated at a frequency of 120 Hz. The photocurrent was measured using a lock-in amplifier (Stanford Research Systems SR865). The laser diode intensity was

adjusted over a five order of magnitude dynamic range by controlling the laser current in combination with the use of neutral density filters in the beam path. The 3dB frequency analysis was performed with a λ = 1.6 μm laser diode, directly modulated with a sinusoidal waveform.

AUTHOR INFORMATION

Corresponding Author

*E-mail: ajavey@berkeley.edu

Acknowledgements

The authors would like to acknowledge P. Wijewarnasuriya and E. DeCuir from the U.S. Army Research Laboratory for their discussions. This work was supported by the Defence Advanced Research Projects Agency under contract no. HR0011-16-1-0004. K.B.C. acknowledges funding from the Australian Research Council (DP150103736 and FT140100577) and an Innovation Fellowship from the Victorian Endowment for Science, Knowledge and Innovation (VESKI).

Author Contributions

J.B., M.A. and A.J. conceived the idea for the project and designed the experiments. J.B. and M.A. performed optical measurements. M.A., J.B., J.C., and G.H.A. fabricated devices. V.A. performed device simulations. Y.-Z.C. and Y.-L.C. performed TEM measurements. J.B, M.A., V.A., V.R.S., Y.G., K.B.C. and A.J. analysed the data. J.B., M.A., and A.J. wrote the manuscript. All authors discussed the results and commented on the manuscript.

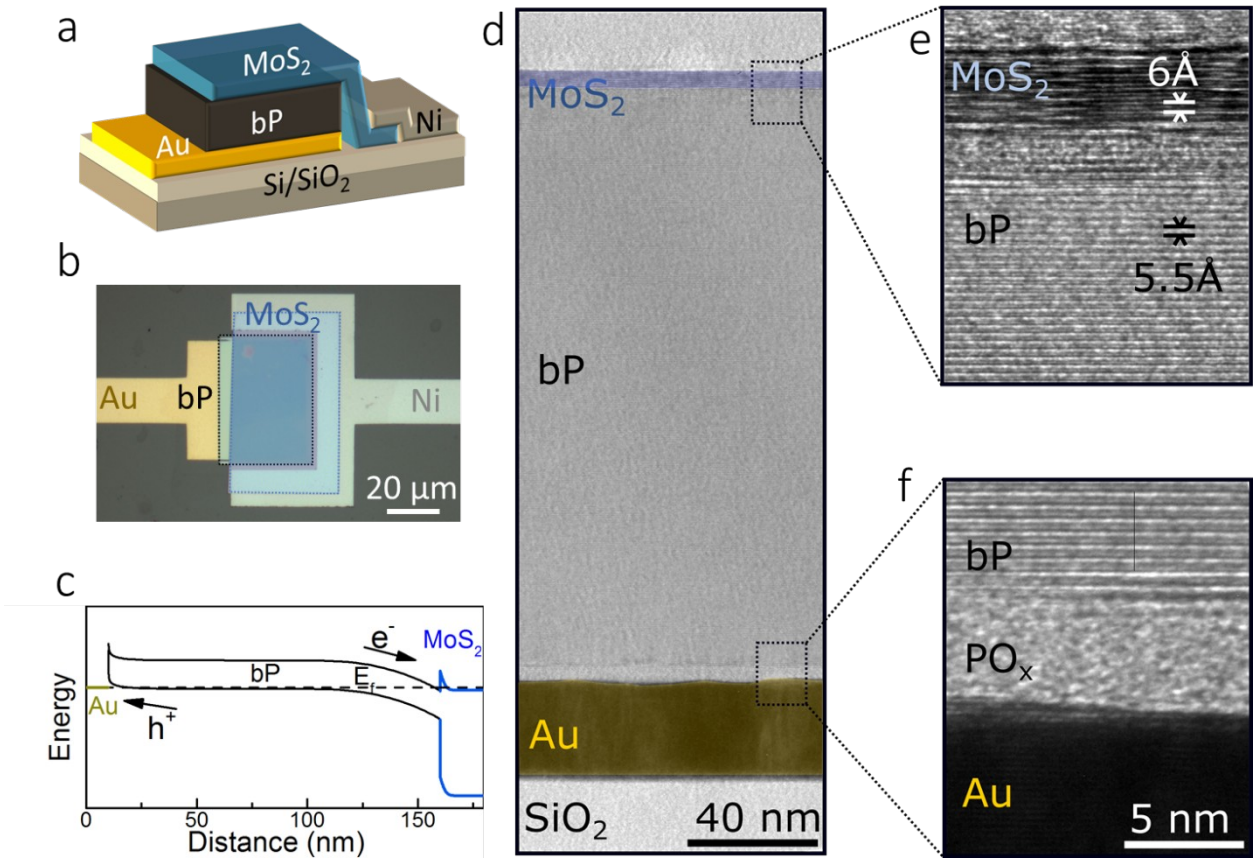

Fig. 1 | bP/MoS_2 heterojunction photodiode. **a**, Schematic of device configuration, showing the heterojunction and contact configuration. **b**, Optical micrograph of a completed device, regions containing bP and MoS_2 are outlined for clarity. **c**, Simulated energy band diagram of the device under equilibrium. **d**, Cross-sectional TEM image of a completed photodiode. **e**, High resolution cross-sectional TEM image showing the bP/MoS_2 interface. **f**, High resolution cross-sectional TEM image showing the bP/Au interface.

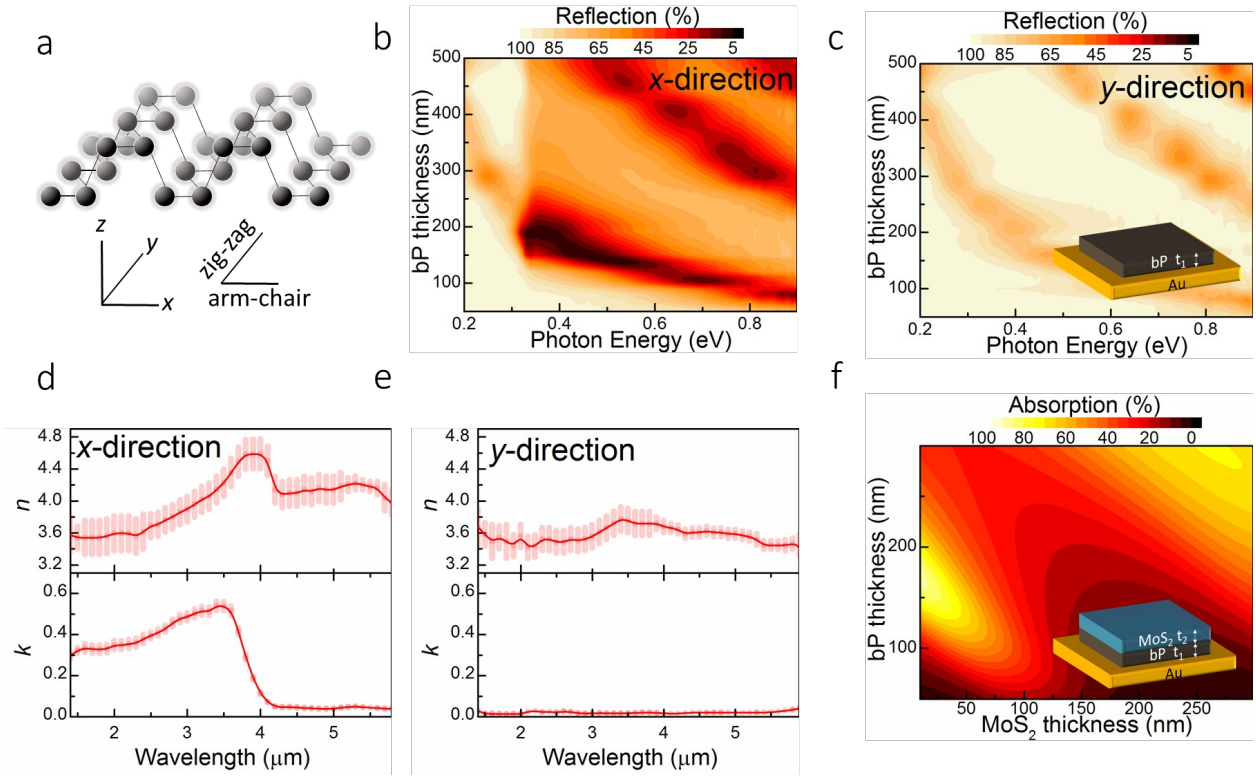

480**Fig. 2 | Infrared optical constants of bP. a**, Schematic diagram of bP
481crystal structure, **b**, Reflection of bP on Au, measured for crystals with
482thickness ranging from 50 nm to 500 nm with the polarizer aligned in the *x*-
483direction. **c**, Reflection of bP on Au, measured for crystals with thickness
484ranging from 50 nm to 500 nm with the polarizer aligned in the *y*-direction.
485**d**, Extracted complex refractive index of bP in the *x*-direction. **e**, Extracted
486complex refractive index of bP in the *y*-direction. Error bars in d and e are
487based on the deviation between the modelled and measured reflection at
488each wavelength. **f,** Modelled absorption in bP layer, for a bP / MoS_2 stack on
489Au, as a function of the bP and MoS_2 layer thicknesses.

490

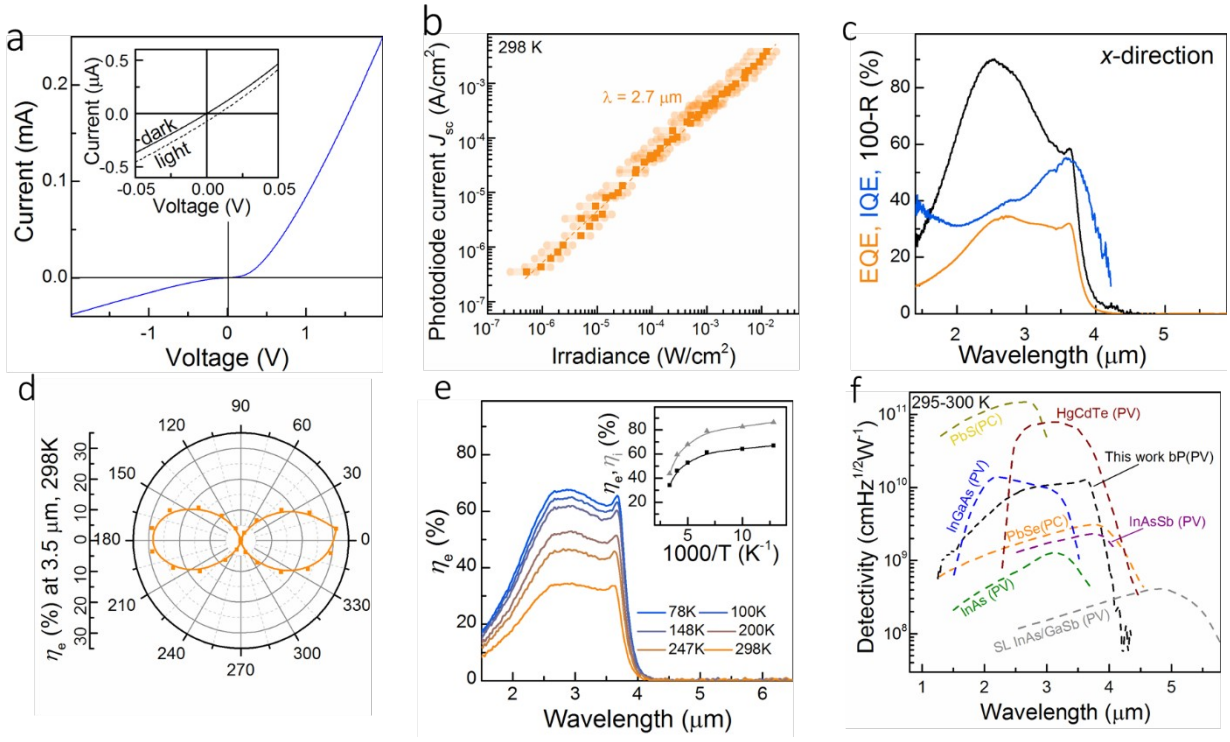

Fig. 3 | Photoresponse and detectivity. **a**, *IV* curve of a bP/MoS_2 heterojunction photodiode; inset shows measurement taken in the dark and under illumination by a 1000 K blackbody source over a voltage range of V = ±50 mV. **b**, Measured photocurrent as a function of incident illumination intensity. Excitation is performed with a λ = 2.7 μm laser diode. Error bars are based on the uncertainty in the laser spot size, **c**, spectrally dependent η_e, η_i and 100%-*R* for a bP / MoS_2 heterojunction photodiode, **d**, measured η_e at λ=3.5 μm as a function of polarization angle, **e**, Spectral η_e as a function of temperature. Inset shows η_e and η_i at λ=3 μm as a function of temperature. **f**, Specific detectivity as a function of wavelength measured for a bP / MoS_2 heterojunction at room temperature as well as various commercially available and reported MWIR photodetectors. The shaded

region highlights the MWIR band. All FTIR and laser diode characterization was performed at a device bias of 0 V.

Fig. 4 |

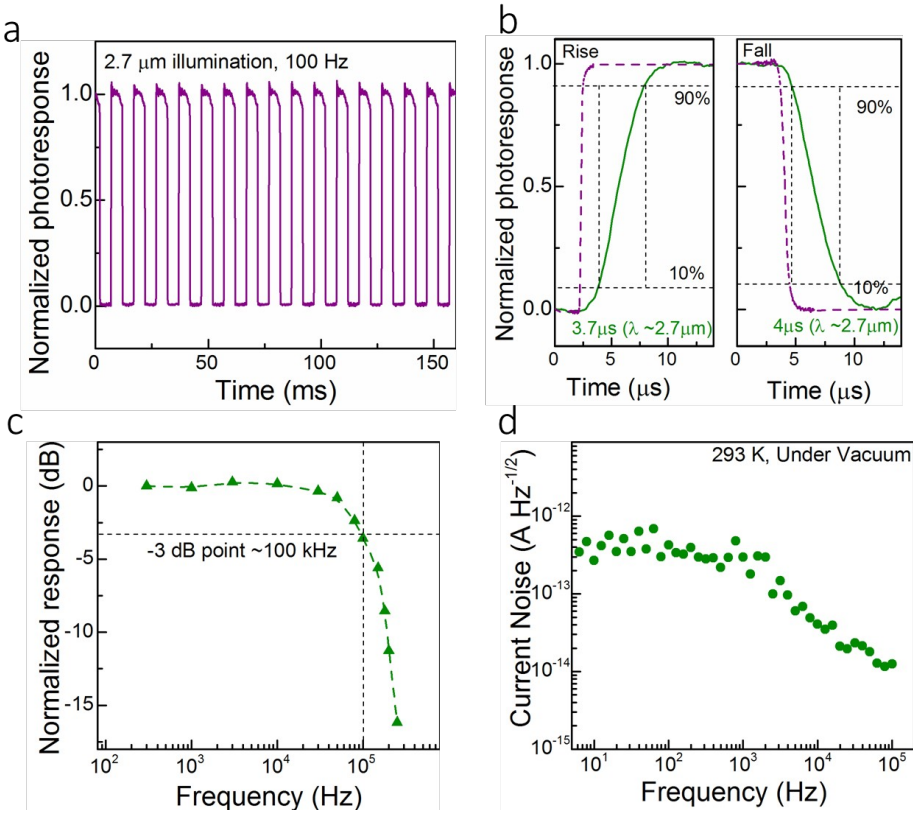

Frequency response and noise. a, Photocurrent measured from a bP / MoS_2 photodiode under a modulated illumination source (λ= 2.7 μm). **b**, 90%-10% rise and fall times measured with a λ= 2.7 μm illumination source (~10 mW/cm^2). Green solid lines are representative of the bP / MoS_2 photodiode and the purple dotted lines show the instrument response (measured using a commercial InAs photodiode, Judson J12D). **c**, Frequency response of a bP / MoS_2 photodiode, showing a 3 dB frequency of 100 kHz (λ=1.6 μm). **d**, Spectral noise density of a bP / MoS_2 photodiode. All device photoresponse and noise characterization was performed at a bias of 0 V.

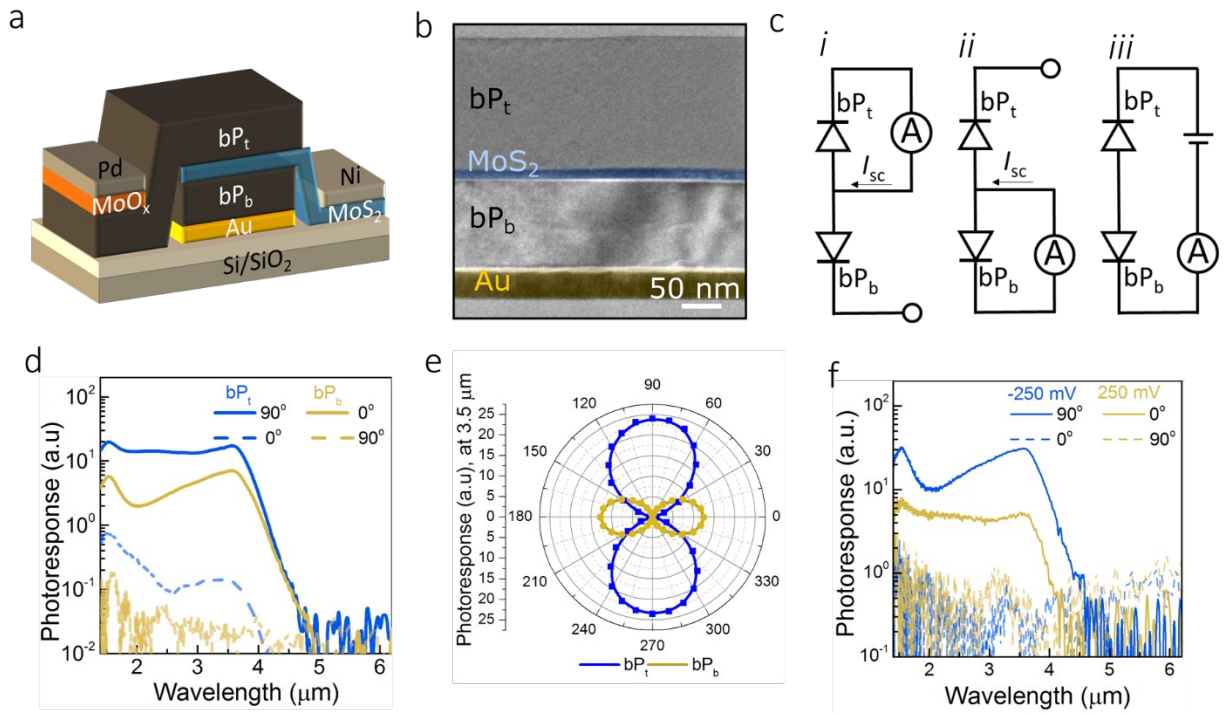

517**Fig. 5 | Polarization resolved bP/MoS$_2$ heterojunction photodiode. a**, 518Schematic of polarization resolved bP/MoS$_2$ heterojunction photodiode, 519showing the heterojunction and contact configuration. **b**, Cross-sectional TEM 520image of a completed polarization resolved bP/MoS$_2$ heterojunction 521photodetector, showing the various layers in the device. **c**, Electrical 522configurations used to measure: photoresponse from bP$_t$ (i), photoresponse 523from bP$_b$ (ii), and photoresponse from the top or bottom mode using the bias 524selectable mode (iii). **d**, Spectrally resolved photoresponse measured from 525bP$_t$ and bP$_b$ under linearly polarized illumination normal and perpendicular to 526the device. **e**, Measured photoresponse under linearly polarized illumination 527at λ = 3 μm in bP$_t$ and bP$_b$ as a function of polarizer angle. **f**, spectrally 528resolved photoresponse of the device in the bias selectable mode under four

different conditions: ±250 mV for polarization aligned to the x-axis of the top and bottom devices.

References

1. Xia, F., Wang, H., Xiao, D., Dubey, M. & Ramasubramaniam, A. Two-dimensional material nanophotonics. *Nat. Photonics* **8,** 899–907 (2014).
2. Jakšić, Z. *Micro and Nanophotonics for Semiconductor Infrared Detectors*. (Springer-Verlag, 2014).
3. Rogalski, A., Adamiec, K. & Rutkowski, J. *Narrow-Gap Semiconductor Photodiodes*. (SPIE Press, 2000).
4. Wang, X., Cheng, Z., Xu, K., Tsang, H. K. & Xu, J.-B. High-responsivity graphene/silicon-heterostructure waveguide photodetectors. *Nat. Photonics* **7,** 888–891 (2013).
5. Xia, F., Wang, H. & Jia, Y. Rediscovering black phosphorus as an anisotropic layered material for optoelectronics and electronics. *Nat. Commun.* **5,** 5458 (2014).
6. Ling, X., Wang, H., Huang, S., Xia, F. & Dresselhaus, M. S. The renaissance of black phosphorus. *Proc. Natl. Acad. Sci.* **112,** 4523–4530 (2015).
7. Yuan, H. *et al.* Polarization-sensitive broadband photodetector using a black phosphorus vertical p–n junction. *Nat. Nanotechnol.* **10,** 707–713 (2015).
8. Qiao, J., Kong, X., Hu, Z.-X., Yang, F. & Ji, W. High-mobility transport anisotropy and linear dichroism in few-layer black phosphorus. *Nat. Commun.* **5,** 5475 (2014).
9. Hong, T. *et al.* Anisotropic photocurrent response at black phosphorus–MoS2 p–n heterojunctions. *Nanoscale* **7,** 18537–18541 (2015).
10. Deng, Y. *et al.* Black Phosphorus–Monolayer MoS2 van der Waals Heterojunction p–n Diode. *ACS Nano* **8,** 8292–8299 (2014).

55611. Ye, L., Li, H., Chen, Z. & Xu, J. Near-Infrared Photodetector Based on
557 MoS2/Black Phosphorus Heterojunction. *ACS Photonics* **3,** 692–699 (2016).
55812. Chen, P. *et al.* Gate tunable WSe2–BP van der Waals heterojunction devices.
559 *Nanoscale* **8,** 3254–3258 (2016).
56013. Shim, J. *et al.* Phosphorene/rhenium disulfide heterojunction-based negative
561 differential resistance device for multi-valued logic. *Nat. Commun.* **7,** 13413
562 (2016).
56314. Huang, M. *et al.* Broadband Black-Phosphorus Photodetectors with High
564 Responsivity. *Adv. Mater.* **28,** 3481–3485 (2016).
56515. Youngblood, N., Chen, C., Koester, S. J. & Li, M. Waveguide-integrated black
566 phosphorus photodetector with high responsivity and low dark current. *Nat.*
567 *Photonics* **9,** 247–252 (2015).
56816. Guo, Q. *et al.* Black Phosphorus Mid-Infrared Photodetectors with High Gain.
569 *Nano Lett.* **16,** 4648–4655 (2016).
57017. Mao, N. *et al.* Optical Anisotropy of Black Phosphorus in the Visible Regime. *J.*
571 *Am. Chem. Soc.* **138,** 300–305 (2016).
57218. Liu, H. *et al.* Phosphorene: An Unexplored 2D Semiconductor with a High Hole
573 Mobility. *ACS Nano* **8,** 4033–4041 (2014).
57419. Tran, V., Soklaski, R., Liang, Y. & Yang, L. Layer-controlled band gap and
575 anisotropic excitons in few-layer black phosphorus. *Phys. Rev. B* **89,** 235319
576 (2014).
57720. Li, D. *et al.* Polarization and Thickness Dependent Absorption Properties of
578 Black Phosphorus: New Saturable Absorber for Ultrafast Pulse Generation. *Sci.*
579 *Rep.* **5,** 15899 (2015).
58021. Macleod, A. *Thin-Film Optical Filters*. (CRC Press, 2010).

58122. Villegas, C. E. P., Rocha, A. R. & Marini, A. Anomalous Temperature
582 Dependence of the Band Gap in Black Phosphorus. *Nano Lett.* **16,** 5095–5101
583 (2016).
58423. Villegas, C. E. P., Rodin, A. S., Carvalho, A. & Rocha, A. R. Two-dimensional
585 exciton properties in monolayer semiconducting phosphorus allotropes. *Phys.*
586 *Chem. Chem. Phys.* **18,** 27829–27836 (2016).
58724. Li, L. *et al.* Quantum Hall effect in black phosphorus two-dimensional electron
588 system. *Nat. Nanotechnol.* **11,** 42 (2016).
58925. Martyniuk, P., Kopytko, M. & Rogalski, A. Barrier infrared detectors. *Opto-*
590 *Electron. Rev.* **22,** 127–146 (2014).
59126. Dhar, N. K., Dat, R. & Sood, A. K. Advances in Infrared Detector Array
592 Technology. in *Optoelectronics - Advanced Materials and Devices* (InTech, 2013).
59327. Amani, M., Regan, E., Bullock, J., Ahn, G. H. & Javey, A. Mid-Wave Infrared
594 Photoconductors Based on Black Phosphorous-Arsenic Alloys. *ACS Nano* (2017).
595 doi:10.1021/acsnano.7b07028
59628. Buscema, M. *et al.* Fast and Broadband Photoresponse of Few-Layer Black
597 Phosphorus Field-Effect Transistors. *Nano Lett.* **14,** 3347–3352 (2014).
59829. Martyniuk, P. & Rogalski, A. HOT infrared photodetectors. *Opto-Electron. Rev.*
599 **21,** 239–257 (2013).
60030. Yau, L. D. & Sah, C.-T. Theory and experiments of low-frequency generation-
601 recombination noise in MOS transistors. *IEEE Trans. Electron Devices* **16,** 170–
602 177 (1969).
60331. Haddadi, A., Dehzangi, A., Chevallier, R., Adhikary, S. & Razeghi, M. Bias–
604 selectable nBn dual–band long–/very long–wavelength infrared photodetectors

605 based on InAs/InAs 1−x Sb x /AlAs 1−x Sb x type–II superlattices. *Sci. Rep.* **7,**
606 3379 (2017).
60732. Bullock, J., Cuevas, A., Allen, T. & Battaglia, C. Molybdenum oxide MoOx: A
608 versatile hole contact for silicon solar cells. *Appl. Phys. Lett.* **105,** (2014).
60933. Chuang, S. *et al.* MoS2 P-type Transistors and Diodes Enabled by High Work
610 Function MoOx Contacts. *Nano Lett.* **14,** 1337–1342 (2014).
61134. Low, T. *et al.* Tunable optical properties of multilayer black phosphorus thin
612 films. *Phys. Rev. B* **90,** 075434 (2014).
61335. Morita, A. Semiconducting black phosphorus. *Appl. Phys. A* **39,** 227–242
614 (1986).
61536. Huang, Y. *et al.* An innovative way of etching MoS<Subscript>2</Subscript>:
616 Characterization and mechanistic investigation. *Nano Res.* **6,** 200–207 (2013).